Volume 19, Number 1, 2026. pp. 41-53

Jordan Journal of Physics

ARTICLE

Structural, Optical, and Magnetic Properties of (Ca, V) Co-doped ZnO Nanopowder Prepared by a Modified Sol-gel Technique

S. Mrabet[a], **C. Vazquez Vazquez**[b], **N. Ihzaz**[a,c], **M. N. Bessadok**[a], **D. Ananias**[d], **J.S. Amaral**[d], **M. Nouiri**[a], **A. Bouloufa**[e], **Z. Ben Ayadi**[a] and **L. El Mir**[a]

[a] *Laboratory of Physics of Materials and Nanomaterials applied at Environment (LaPhyMNE) LR05ES14, Faculty of Sciences of Gabes, Gabes University, Erriadh City, Zrig, 6072 Gabes, Tunisia.*

[b] *NANOMAG laboratory, Institut of ceramica,University of Santiago de compostela, Galicia, Spain.*

[c] *Laboratory of Physico-Chemistry of Materials, Department of Physics, Faculty of Sciences, 5000 Monastir, Tunisia.*

[d] *Department of Physics, CICECO – Aveiro Institute of Materials, University of Aveiro, 3810-193 Aveiro, Portugal.*

[e] *Laboratory of Electrochemistry and Materials, University Ferhat Abbas Sétif-1, Algeria.*

DOI: **https://doi.org/10.47011/19.1.5**

Received on: 05/11/2024; *Accepted on: 25/03/2025*

Abstract: (Ca,V) co-doping effects on the structural, optical, and magnetic properties of zinc oxide nanoparticles (NPs) were explored. The nanoparticles were synthesized via a modified sol-gel route. X-ray diffraction analysis confirms the hexagonal polycrystalline wurtzite phase. No segregated secondary phases or Ca/V-rich clusters were detected. Morphological observations were carried out by scanning electron microscopy (SEM) and transmission electron microscopy (TEM). EDS analysis revealed the existence of all elements in all the regions of the sample. TEM images show an almost prismatic cylindrical shape of the nanoparticles. Optical studies carried out by UV-Vis spectroscopy indicated a decrease in the value of the band gap after (Ca,V) incorporation. Magnetic measurements reveal a clear hysteresis showing the ferromagnetic behavior of this kind of material. These results are very promising for many technological applications such as hyperthermia, gas sensors, and optoelectronics.

Keywords: (Ca,V) co-doped zinc oxide, Nanoparticles, Sol-gel technique, Photoluminescence, Magnetic properties.

1. Introduction

Over time, there has been growing interest in bulk and nanostructured diluted magnetic semiconductors (DMS). They have been stimulated thanks to their outstanding, distinguished, and exceptional chemical, optical, and magnetic properties which makes them promising raw candidate materials for user-friendly multifunctional devices such as sensors, transistors, diodes, photocatalysis, optoelectronic and spintronic devices [1]. The suitability of DMS for spintronic applications arises from their ability to incorporate magnetic ions, which is a small amount of host matrix cations. In this line, many works have been dedicated to exploring the magnetic properties of IV, III-V, and II-VI materials doped with magnetic cations [2]. In this respect, zinc oxide (ZnO) stands out as a candidate material owing to its wide band gap, with a bandwidth equal to 3.37 eV at room temperature [3], classifying it as a typical model

Corresponding Authors: Sihem Mrabet **Email**: sihem.mrabet@fsg.rnu.tn
Lassaad EL MIR **Email**: Lassaad.ElMir@fsg.rnu.tn

of the third–generation semiconductor material and also exhibits high exciton binding energy about 60 meV [4]. In addition, it has the characteristics of stable chemical and physical properties, low price, non-toxicity, and environmental friendliness. Besides, the elemental substitution at zinc (Zn) sites in the zinc oxide host matrix prompts significant influence on the optical, luminescence, magnetic, and electrical properties. Thus, the incorporation of foreign dopants into the ZnO matrix alters its near band edge transitions (UV and visible emissions) which leads to the creation of different defect types like zinc interstitial, oxygen vacancies and zinc vacancy oxygen interstitial, which in turn generate the green and red emission and induction of ferromagnetism in diamagnetic zinc oxide lattice [5–14]. Introducing transition metal (TM) tends to cause dramatic changes in optical and electrical properties of a wide band DMS material. Magnetic properties of V-doped ZnO thin films prepared via pulse laser deposition process, nanotube, and rutile TiO_2 have been reported in previous works [15–18]. The theoretical study showed that vanadium doping in semiconducting oxides could conduct RTFM. Xu et al. [19] evoked a ferromagnetism state in V-doped ZnO nanorods. Vyatkin et al. [20] explored the ferromagnetic behaviour in ZnO by V^+ ion implantation. Theoretical study has demonstrated the role of Ca in the ferromagnetism in ZnO [21]. The study of the effect of Ca doping on the magnetic properties of ZnO is limited. In our investigation of the impact of calcium on the physical properties of ZnO, we noticed that calcium introduction into the ZnO matrix creates more oxygen vacancies that lead in turn to the formation of more BMPs which generate the ferromagnetism [22]. Besides, doping with Ca enhances the electrical properties of ZnO by providing one more carrier. According to our previous investigations; doping with V enhances the optical and magnetic properties. It is known that vanadium is an optical activator to ZnO [22] and Ca is a disruptive element to ZnO that creates more $V_{O,}$ so the idea to investigate the effect of dual doping with Ca and V on the optical and magnetic properties of ZnO. The origin of ferromagnetism in DMS is still under discussion and the role of native defects such as oxygen vacancies in the ferromagnetic behaviour in this kind of materials should be taken into account. In this work, we reported the effect of Ca and V on the structural, optical, luminescence, and magnetic properties of (Ca,V) co-doped ZnO nanoparticles. The examination of the particle size of our nanoparticles acquired from direct powder X-ray diffraction (XRD) peak is reported. The UV-visible optical absorption was used to confirm the substitution of both Ca and V ions within the Zn ones matching with the bandgap shifting. Photoluminescence spectra are accomplished to identify existing defects. A vibrating sample magnetometer (VSM) was utilized to evaluate the variation of magnetization with temperature and field. The evolution of magnetization with temperature and magnetic field was investigated.

2. Experimental Details

Vanadium and calcium co-doped zinc oxide nanoparticles were synthesized using the sol-gel process following El Mir et al. protocol [23, 24]. As primary precursors zinc acetate dehydrate, ammonium metavanadate (NH_4VO_3), and calcium chloride ($CaCl_2{\cdot}6H_2O$), purchased from Sigma-Aldrich were used. The synthesis procedure is straightforward and begins with dissolving the precursors in methanol, under magnetic stirring and the obtained solution is transferred into an autoclave under the supercritical drying conditions of ethyl alcohol; after five hours, we obtain the desired nanopowder. The specimens were investigated by X-ray diffraction (XRD) using a Bruker D8 Advance diffractometer, with Cu-Kα radiation (1.54186 Å), in the range 10 to 80 °C, with a step of 0.03º and 5s/step. Transmission electron microscopy (TEM) micrographs were acquired by JEOL JEM1011 electron microscope, at an acceleration voltage of 100 kV. Samples for TEM analysis were made by placing a drop (20 µL) of an aqueous dispersion of the nanoparticles onto a 400 mesh copper grid coated with an amorphous carbon film, supported on paper filter, and left to evaporate at room temperature. SEM images were obtained using a ZEISS UltraPlus FESEM microscope equipped with an EDS analyzer. Chemical composition and their atomic concentrations were studied using energy dispersive spectroscopy (EDS). Optical properties have been explored by a UV-visible-IR spectrometer (Shimadzu UV-3101PC) coupled with an integrated sphere in the wavelength range from 200 to 2400 nm. The PL spectrophotometer was carried out to study the intrinsic and extrinsic properties of ZnO at room temperature and magnetic measurements were carried out by VSM.

3. Results and Discussion

3.1. Structural Properties

Figure 1 illustrates the X-ray diffraction peaks of ZnV (ZnO:V with V 3 at.%), ZnCa (ZnO:Ca with Ca 4 at.%), and ZnVCa (ZnO:(Ca,V) with V 3 at.% and Ca 4 at.%) nanoparticles. Six pronounced diffraction peaks corresponding to the (100), (002), (101), (102), (110) and (103) planes were detected. The well-defined peaks and their intensities were compared and matched to the standard JCPDS database card (card no: 36-1451) confirming the development of hexagonal crystalline phase with $P6_3mc$ space group and wurtzite structure definite for ZnO material in ambient pressure and temperature conditions. The crystalline structure was identified as a single phase in ZnV, ZnCa, and ZnVCa NPs without revealing any extra peak related to calcium and/or vanadium oxides. A close zoom on the (002) peak position, illustrated in Fig. 2, shows that this peak position shifted to higher diffraction angles for the co-doped sample; this mismatch in peak positions indicates the well substitution of Ca and V within Zn into the ZnO matrix. As it is known, introducing Ca and V specimens into the ZnO matrix yields a lattice perturbation which is explained by the produced stress. Lattice parameters a and c were calculated by the Eqs. (1) and (2) [25]:

$$a = \frac{\lambda}{\sqrt{(3)}(\sin \theta_{100})} \tag{1}$$

$$c = \frac{\lambda}{\sin \theta_{002}} \tag{2}$$

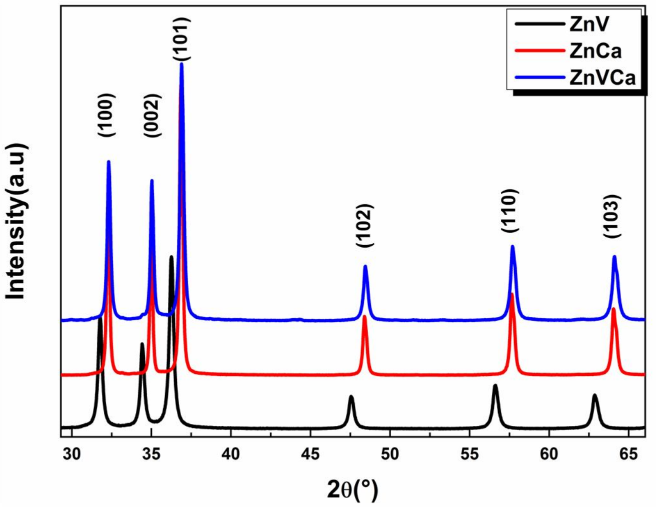

FIG. 1. XRD diffractograms of ZnV, ZnCa, and ZnVCa.

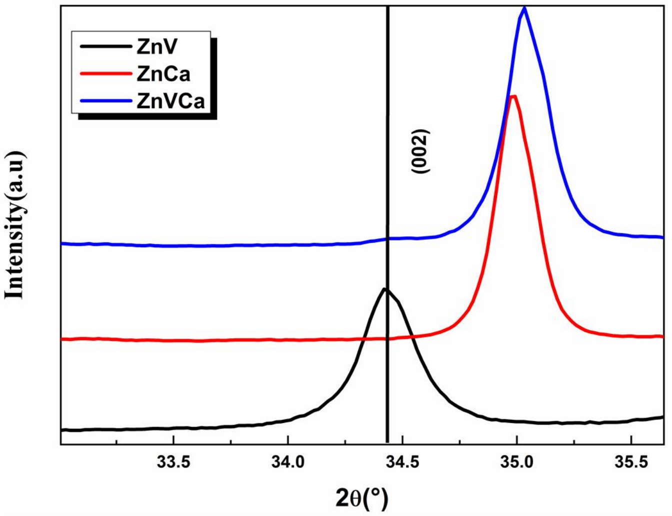

FIG. 2. Zoom of (002) peak.

In Table 1, we flaunt the relevant structural parameters of ZnV, ZnCa, and ZnVCa contents offered by X-ray diffraction data.

TABLE 1. Structural parameters of ZnV, ZnCa and ZnVCa.

Sample	a(Å)	c(Å)
ZnV_3	3.2325	5.1804
$ZnCa_4$	3.2325	5.1808
$Zn(V_3,Ca_4)$	3.2438	5.1977

3.2. Morphology Analysis and Crystallite Size

To explore the average crystallite size of the as-prepared samples, Williamson-Hall (W-H) was employed, in which the crystallite size can be deduced from the linear fit of the following equation [26]:

$$\beta_{hkl}\cos\theta = (k\lambda/D) + (4\varepsilon\sin\theta) \tag{3}$$

It is very important to rectify the instrumental enlargement β_{hkl} for each peak using the next relation:

$$\beta_{hkl} = \sqrt{(\beta_{hkl}^2 - \beta_{inst}^2)} \tag{4}$$

In the W–H model, it is assumed that the strain is uniform in the different crystallographic axis depending on the crystal isotropic character meaning that the material's properties are independent of the direction in which they have been measured. The W-H plot of the as-prepared specimen is represented in Fig. 3. The calculated average crystallite size and the produced stress are regrouped in Table 2.

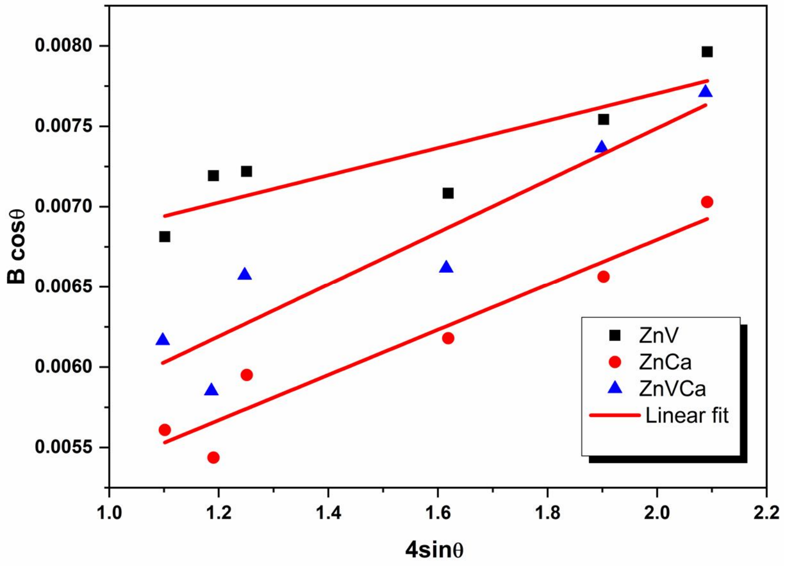

FIG. 3. Williamson–Hall plot ZnO nanoparticles.

TABLE 2. Crystallite size and strain values obtaoned by W-H method.

Sample	$D_{W\text{-}H}$ (nm)	ε (10^{-4})
ZnV_3	23	8
$ZnCa_4$	35	14
$Zn(V_3,Ca_4)$	33	16

Figure 4 shows TEM images of the prepared specimens. It is found that the obtained grain sizes are about 23, 35, and 33 nm for ZnV, ZnCa, and ZnVCa, respectively; which agree well with what were obtained by the W-H method. Looking into these micrographics, we highlight that the various sizes favour coalescence showing visible agglomerates as confirmed by SEM images (Fig. 5 (a, b, c)) which is habitual in this synthesis process [27, 28]. The presence of calcium and vanadium in the case of co-doped specimens was highlighted by EDS analysis during SEM investigations (Fig. 5(d)).

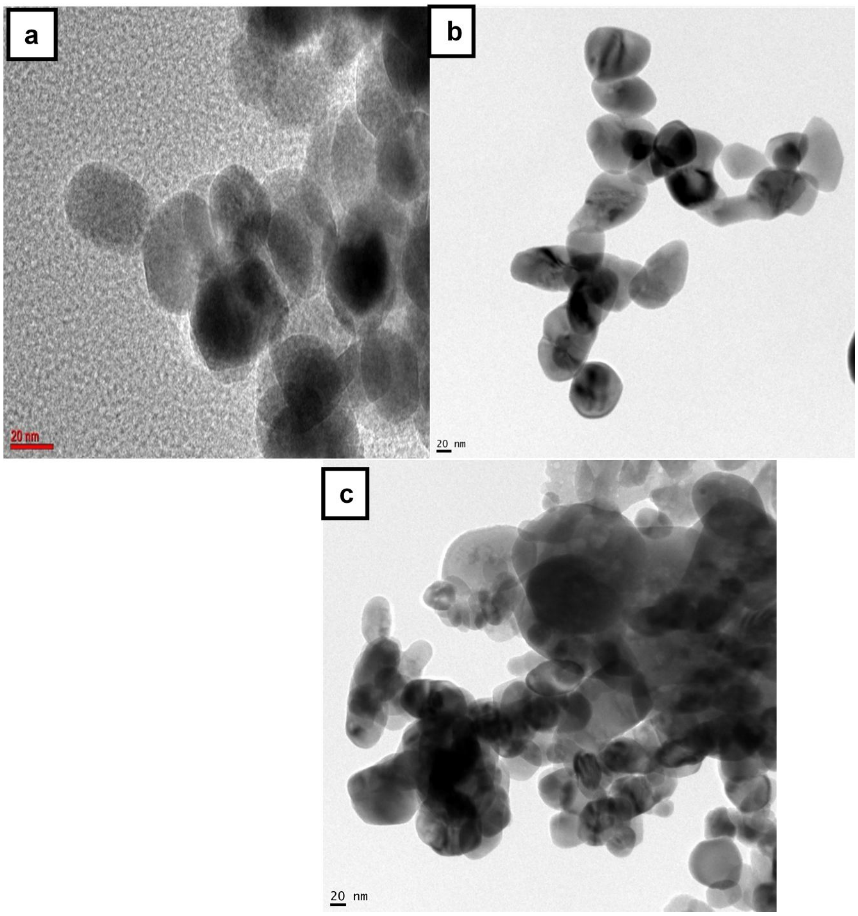

FIG. 4. TEM images of (a) ZnV, (b) ZnCa, (c) ZnVCa specimens.

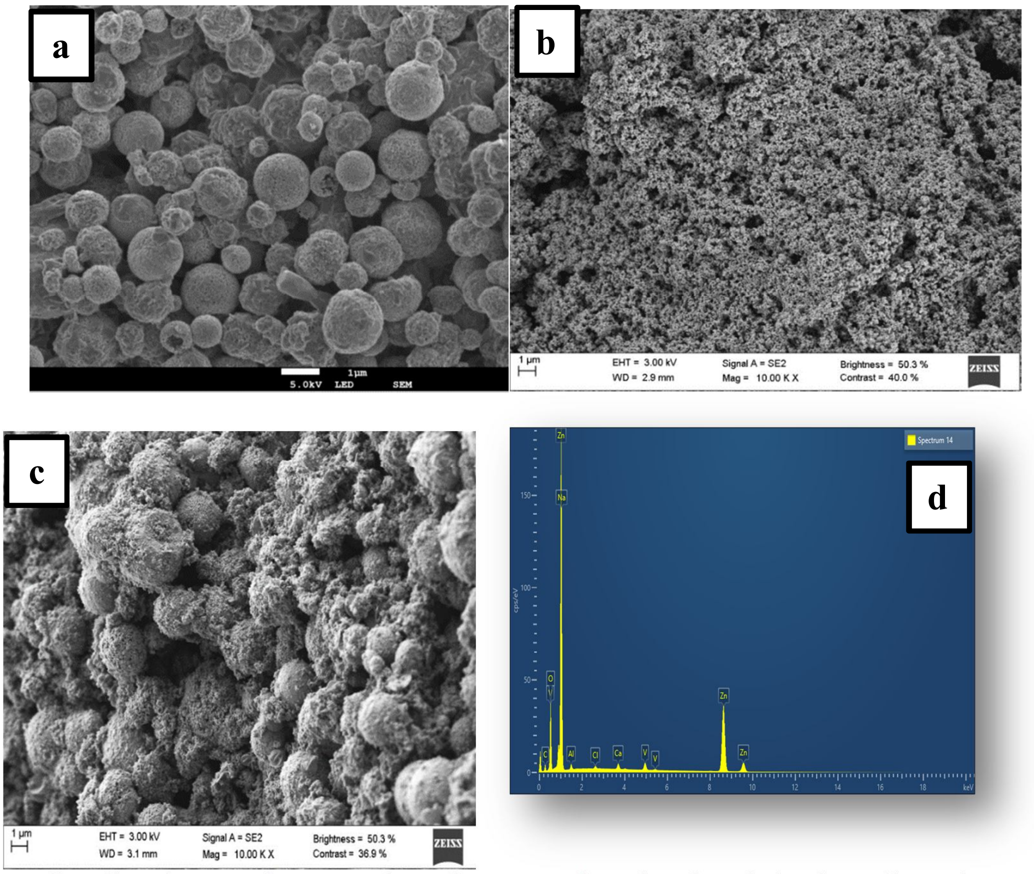

FIG. 5. SEM images of (a) ZnV, (b) ZnCa, (c) ZnVCa and EDS analysis of ZnVCa specimens.

3.3. Optical Properties

3.3.1. UV-VIS Spectroscopy

Figure 6 illustrates the absorption spectra of ZnV, ZnCa, and ZnVCa. All spectra indicate absorption edges in the UV range, which correspond to the optical gap of zinc oxide. An enhancement in visible-range absorption is observed after the co-doping process, which may be linked to size-related effects or caused by the level of impurities caused by doping. The optical bandgaps for all samples were evaluated via the Tauc relation (Eq. 5) [29] by plotting $(\alpha h\upsilon)^2$ versus (hυ), as shown in Fig. 7.

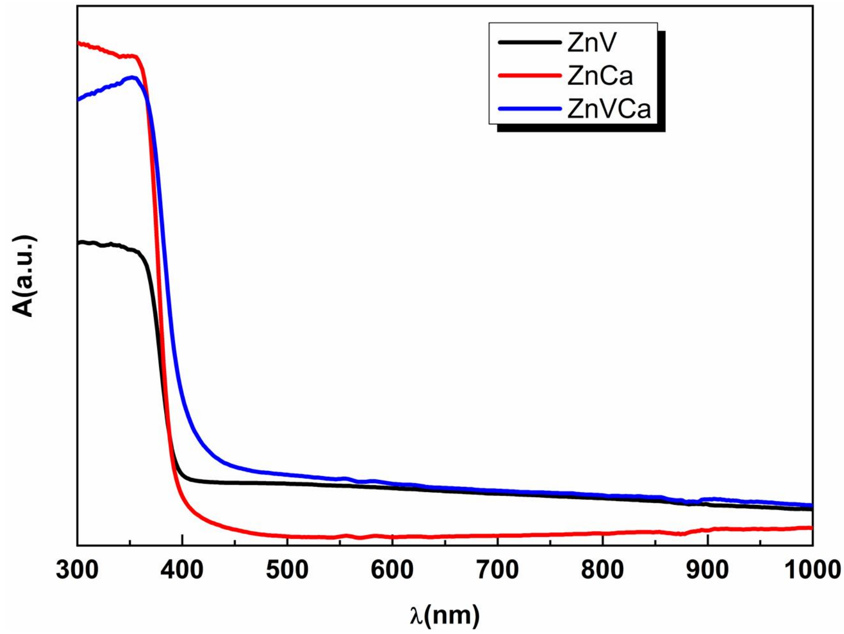

FIG. 6. Absorbance bands of ZnV, ZnCa and ZnVCa samples.

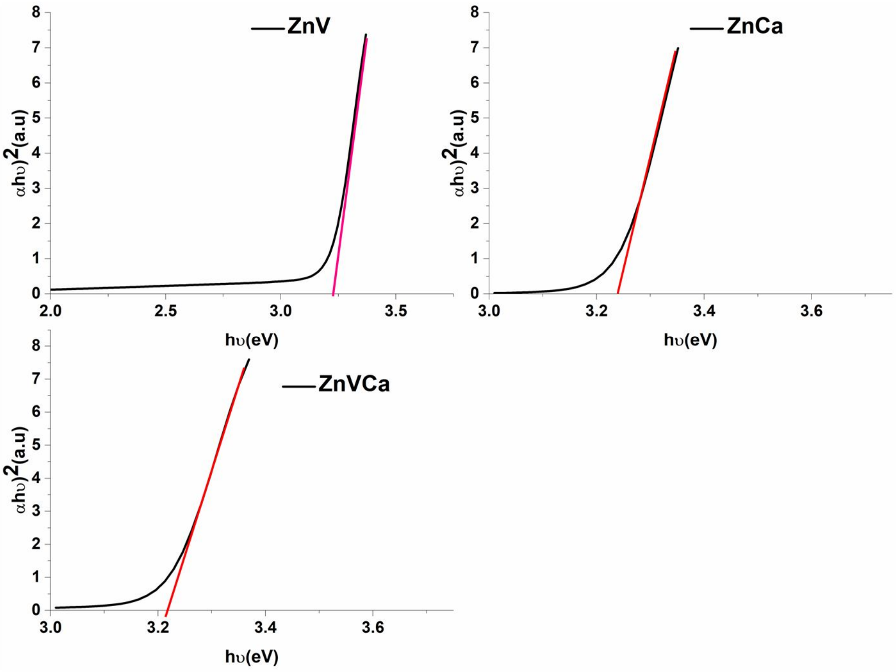

FIG. 7. Band gap of the samples.

$$(\alpha h\nu) = A(h\nu - E_g)^{1/2} \tag{5}$$

where A is a constant, α represents the absorption coefficient, and hν represents the photon energy. The extrapolation of the linear region to the horizontal axis determines the value of the bandgap energy (*E*g) of each specimen. The obtained *E*g values are 3.26, 3.24, and 3.22 eV for ZnV, ZnCa, and ZnVCa respectively. The explanation of the variation of the gap energy as a function of growth parameters and material properties is well known. Indeed; the variation of the band gap with crystallite size in the case of non-homogeneous particle size distribution can be estimated through Eq. (6):

$$E_g = E_g(\propto) + E_b\left(\frac{\pi a_b}{R}\right)^2 \qquad (6)$$

where Eg represents the optical energy gap, Eg (∞) is the bulk bandgap energy (3.35 eV), E_b is the exciton binding energy (60 meV), a_b represents the exciton Bohr radius (2 nm in the case of ZnO), and R is the nanocrystallite radius (D/2). In our case, the variation of the bandgap can be interpreted by the estimation given in Eq. 6 even though the half crystallite size (*D*/2) of as-prepared samples surpasses the Bohr radius, by taking into consideration the non-homogeneous particle size distribution [30, 31]. The addition of charge compensators generates a slight decrease in the bandgap (these are possibly to be a result of charge compensators that occupy Zn^{+2} sites) generating oxygen vacancies to build shallow donor levels below the conduction band. Thus, consequences generate a red shift of absorption edges and reduce the band gap [32]. Due to the Sp-d orbital, co-doping reduces the bandgap of ZnO; oxygen vacancies may reduce the bandgap of ZnO and also the possibility of the formation of donor-acceptor bands shrinks the bandgap [33]. Kumawat et al. have reported similar narrowing after co-doping with Eu and Li [34]. The observed narrowing in the bandgap's energy following the transition metal (TM) doping process was reported numerous times [35]. The incorporation of V^{2+} and Ca^{2+} into the ZnO matrix generates the formation of a tail state in the proximity of the valence band. A. Saffen et al. [36] reported similar shrinking in the bandgap energy with dual doping with Mn and Co atoms and they allocated it to the band tail effect.

3.3.2. PL Investigations

Photoluminescence spectroscopy was accomplished for all specimens. In general, for zinc oxide material the PL response reveals two kinds of emissions: a near band edge emission in the UV region generally allocated to recombination of free exciton and a second emission obtained from deep-level emission in the visible range: this emission is generated by intrinsic and extrinsic defects.

Figure 8 illustrates the PL response at room temperature of ZnO-doped vanadium nanoparticles with a wavelength excitation of 334 nm. The spectrum exhibits a peak centered at 379 nm attributed to band-to-band emission of ZnO. In addition, a broad visible emission ranging from 400 to 700 nm was observed. Photoluminescence spectroscopy was conducted for ZnCa via an excitation wavelength of 334 nm at room temperature. Fig. 8 shows the PL emission of the as-prepared sample showing a peak at 382 nm corresponding to near band emission (NBE) of zinc oxide. Two extra violet emissions bands located at 408 nm and 436 nm related to an electron transition from a shallow donor level from the neutral zinc interstitials to the high level of the valence band [37]. However, the blue-green emission located at 497 nm which is attributed to transitions involving oxygen vacancies and interstitial oxygen [38]. For the co-doped specimen (ZnVCa), a significant decrease in the intensity of the UV peak located at 385 nm occurred, compared to that obtained in the case of simple doping. For the ZnVCa sample, the intensity becomes lowest highlighting that co-doping boosts the defect concentration. Therefore, the recombination process is dominated by a nonradiative one. In addition to the UV emission, a violet-blue emission centered at almost 456 nm, which may be due to electronic transitions between the zinc interstitial level and the valence band or may be matched with the Zn vacancy level and the bottom of the conduction band [39]. Similar behavior has been reported by Ali et al. [40] besides a broad visible emission, which is evident in Fig. 8.

Visible emission was illustrated in the three specimens with relatively different intensities. It was found that green emission is, generally, associated with oxygen deficiency, although oxygen excess yields to the orange-red emission [41]. The origin of the green emission remains a subject of discussion. Several hypotheses have been proposed, such as singly ionized oxygen vacancy [41], recombination centre [42], oxygen antisite [43], and zinc vacancy [44]. The red emission has been attributed to interstitial zinc [45, 46], but the yellow one was commonly ascribed to interstitial oxygen defects [47].

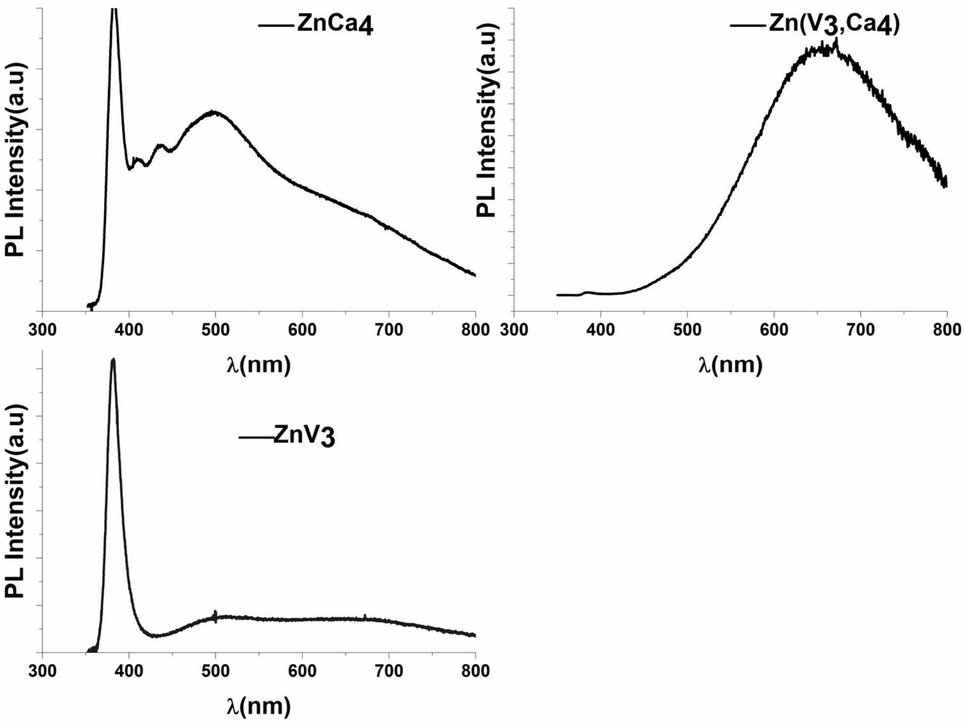

FIG. 8. PL spectra of samples at room temperature.

3.4. Magnetic Properties

The magnetization curves of ZnV, ZnCa, and ZnVCa samples were recorded at 300 K and illustrated in Figs. 9, 10, and 11, respectively. For the ZnV sample, the room temperature magnetization curve indicates at the high fields region an almost linear curve highlighting the paramagnetic/ superparamagnetic response. Moreover, in the low field region, a zoom of the magnetization curve reveals a weak hysteresis loop showing a partial long-range ferromagnetic ordering, which is mainly dictated by the paramagnetic. Even for a 10 kOe applied field, the saturation magnetization is still not attainable due to the paramagnetic component contribution ruled in the high field region. A similar response has been reported for Mn and other MT-doped ZnO systems [48–53]. However, for ZnCa and ZnVCa specimens, the response at high-field regions became diamagnetic and a hysteresis loop was still viewed in the low-field region, highlighting the ferromagnetic response. In the case of co-doping, the remnant magnetization (M_r) increased to $1.3\times10^{-3}\, emu/cm^3$, compared to $1.4\times10^{-4}\, emu/cm^3$ for ZnCa and $3.8\times10^{-4}\, emu/cm^3$ for ZnV. As it is evident from the XRD result that all specimens have a single Wurtzite structure phase without any secondary peaks, we suggest that the viewed ferromagnetic response is from intrinsic interactions. In addition, point defects like Zn interstitial and oxygen vacancies could play a major role in boosting the magnetism, and these defects form bound magnetic polarons that stabilize the ferromagnetic ordering. It has been reported that oxygen vacancies are crucial in the observed ferromagnetism response in DMSs. Thus, the exchange interaction between dopants and oxygen vacancies assembles several dopant spins around the O vacancy forming BMPs which are proportional to the density of oxygen vacancies. The formation of BMPs is quite important to stabilize the ferromagnetism in DMS systems, as reported by several research teams [23, 54].

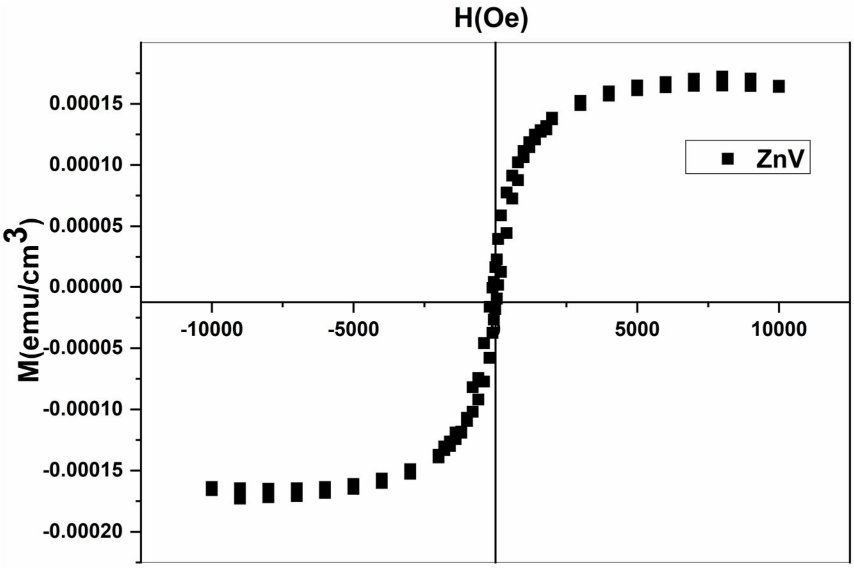

FIG. 9. M-H curve of ZnV at room temperature.

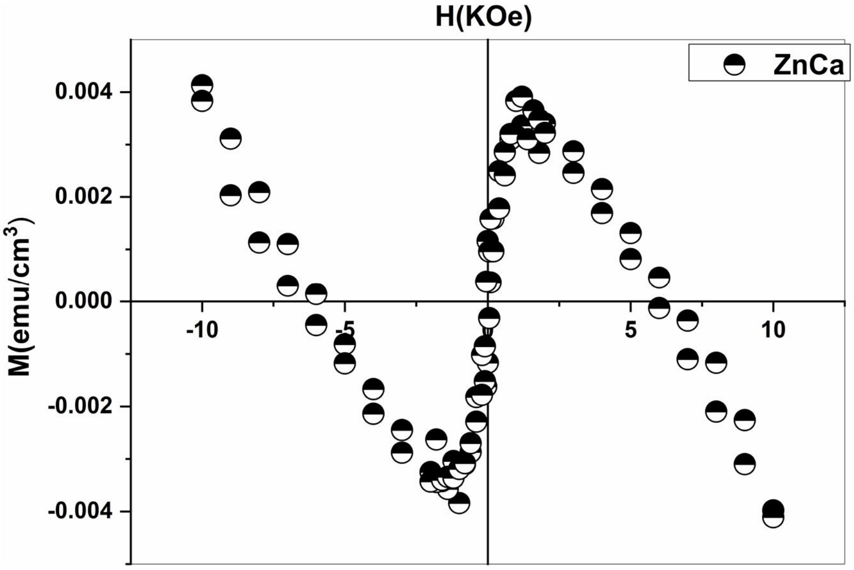

FIG. 10. M-H curve of ZnCa at room temperature.

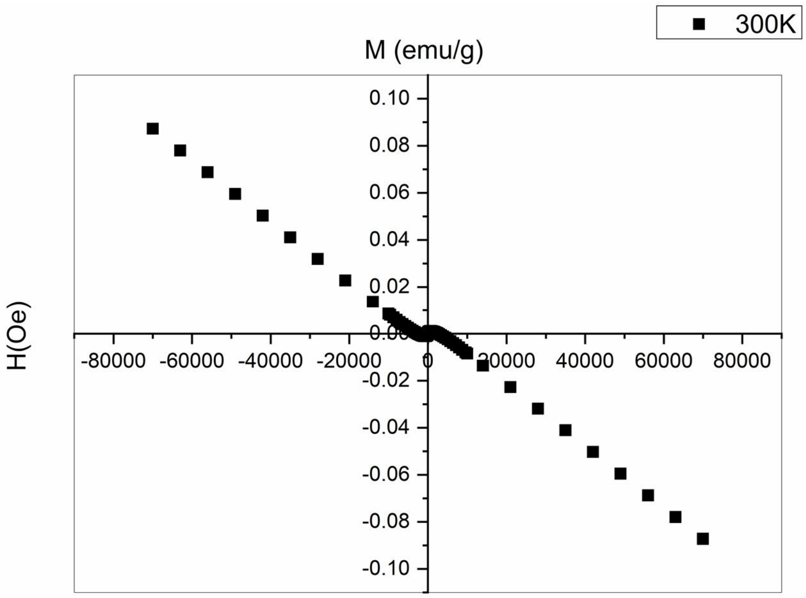

FIG. 11. M-H curve of ZnVCa at room temperature.

For more investigations zero field cooled (ZFC) and field cooled (FC) curves of co-doped sample were conducted. ZFC and FC curves are illustrated in Fig. 12. For the FC magnetization state, the sample has been cooled from 300 K to 10 K under an applied field of 100 Oe and the temperature was saved during the rising of the temperature. It is clear that the bifurcation of FC and ZFC curves starts above 300 K and no sign of blocking temperature can be shown explaining the absence of the superparamagnetic effects at and below 300 K. We represent the thermal evolution of the magnetic susceptibility using the M_{FC} data at 100 Oe in a temperature range from 0 to 300 K in Fig. 13. The experimental data have been fitted by the as given Curie Weiss law (Eq. (7)) [55].

$$\frac{M}{H} = \chi = \frac{C}{T-\theta} \tag{7}$$

where C represents the Curie Weiss constant and θ represents the temperature. The curve highlights two dissimilar slopes owning intercept at the origin and 150 K. The intercept at the origin spotlights the existence of paramagnetic behavior; however, the negative one accentuates the antiferromagnetic behavior. The paramagnetic behavior rules at low-temperature regions. The existence of the antiferromagnetic response in the specimen blocks the entire magnetization value and prevents the ferromagnetic ordering; this explains the obtaining of low saturation and remnant magnetization values and therefore feeble ferromagnetic response. These low values result from the competition between ferromagnetic and antiferromagnetic interactions as indicated in the study of ZnO doped V nanoparticles [22]. For more investigations, we fitted the FC curve by two distinct laws and models namely: Curie Weiss law and standard three-dimensional (3D) spin wave models [56]. As illustrated in Fig. 14, we can't get a relevant fit only by the combination of both models; this means that neither the Curie Weiss law nor the 3D spin wave model can individually fit the FC curve. So the best fit was obtained by a combination of both leading to the adjustment equation (Eq. (8)) [57].

$$M(T) = \frac{CH}{T-\theta} + M_0 - 0.117\mu_B\left(\frac{K_B T}{2SJd^2}\right)^{\frac{3}{2}} \tag{8}$$

where M_0, d and J are zero temperature magnetization, spacing and exchange interaction between magnetic ions, respectively. This combination required the coexistence of both paramagnetic and ferromagnetic contributions in the specimen.

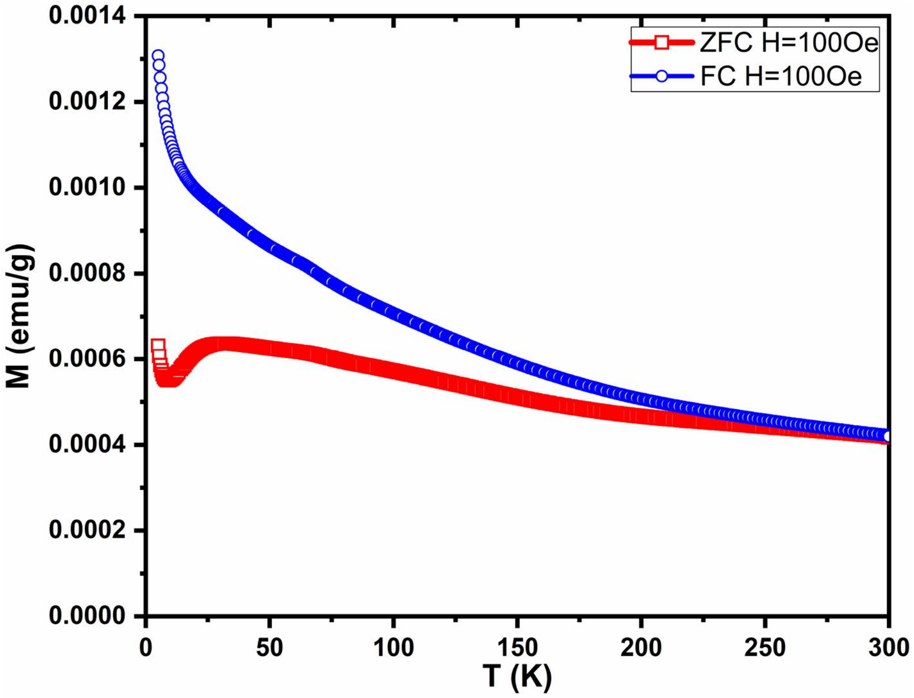

FIG. 12. ZFC and FC curves of ZnVCa sample at 100 Oe.

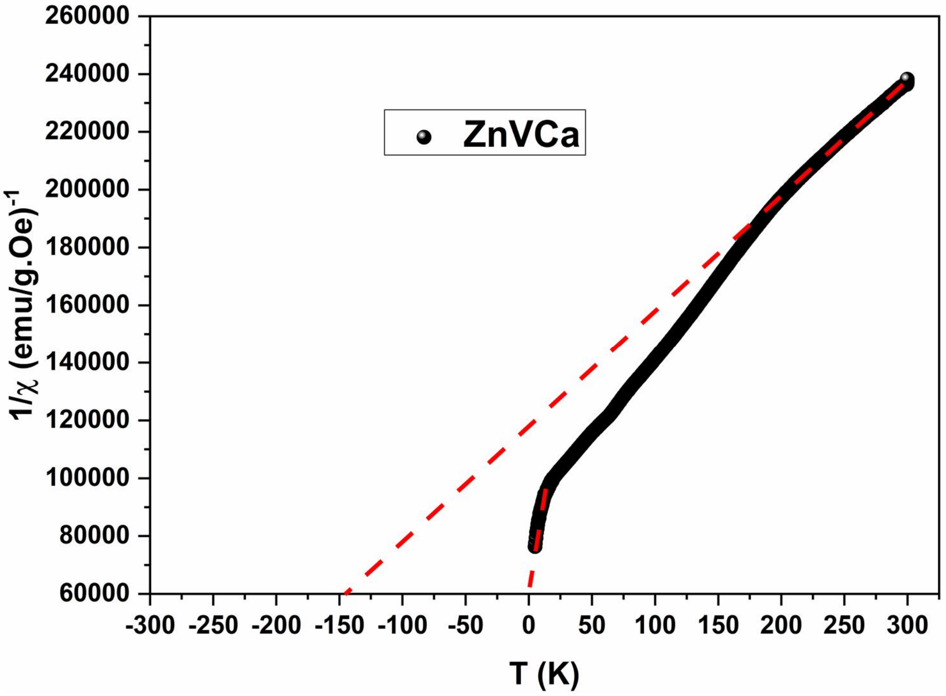

FIG. 13. Variation of inverse of magnetic susceptibility with temperature.

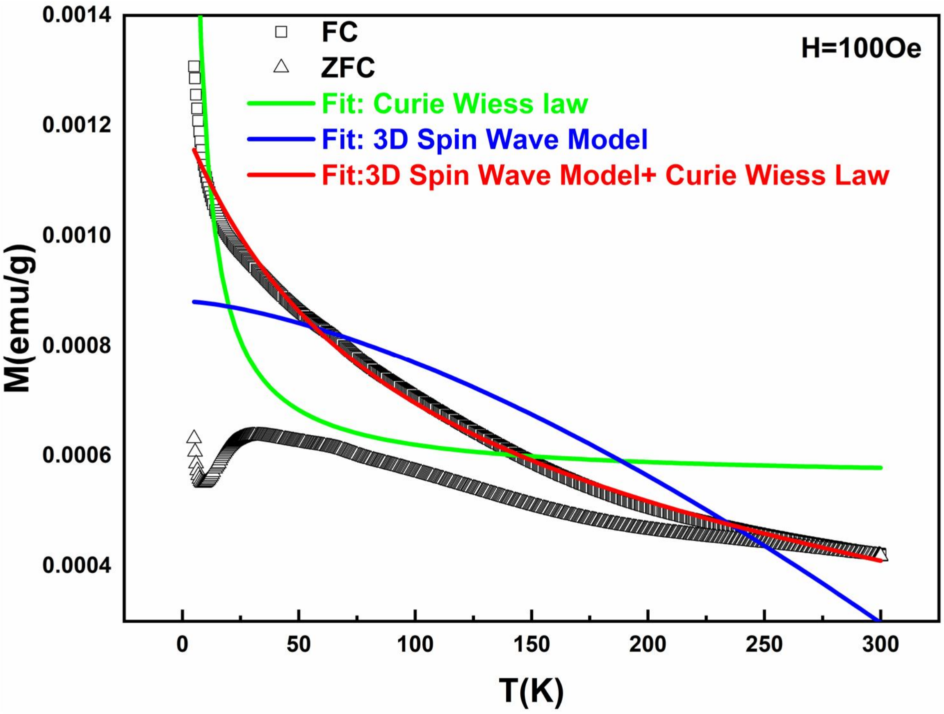

FIG. 14. The fit of FC curve.

4. Conclusion

In conclusion, ZnV, ZnCa, and ZnVCa samples have been synthesized using a modified sol–gel process. XRD diffractograms illustrate a single hexagonal wurtzite phase. UV-Vis spectroscopy reveals a shrinking in the bandgap due to the co-doping process, PL investigations show emissions in the UV and visible range with a significant decrease in the UV peak in the case of co-doping. VSM measurement reveals the co-existence of paramagnetic and ferromagnetic behavior in the vanadium-doped sample. However, we noticed the coexistence of diamagnetic and ferromagnetic behaviors in the other specimens. A special interest was given to the co-doped sample, which is promising for many applications like hyperthermia and optoelectronic devices.

References

[1] Punia, K., Lal, G., Dalela, S., Dolia, S.N., Alvi, P.A., Barbar, S.K., Modi, K.B., and Kumar, S.A., Journal of Alloys and Compounds, 868 (2021) 159142.

[2] Wang, Y., Xiu, F., Wang, Y., Kou, X., Jacob, A.P., Wang, K.L., and Zou, J., Journal of Alloys and Compounds, 508 (2010) 273.

[3] Saravanakumar, B., Mohan, R., Thiyagarajan, K., and Kim, S-J., Journal of Alloys and Compounds, 580 (2013) 538.

[4] El-Hossary, F.M., Mohamed, S.H., Noureldein, E.A., and Abo El-Kassem, M., Materials Science in Semiconductor Processing, 120 (2020) 105284.

[5] Nirmala, M. and Anukaliani, A., Materials Letters, 65 (2011) 2645.

[6] Punia, K., Lal, G., Dolia, S.N., and Kumar, S., Ceramics International, 46 (2020) 12296.

[7] Hjiri, M., Aida, M.S., Lemine, O.M., and El Mir, L., Materials Science in Semiconductor Processing, 89 (2019) 149.

[8] El Ghoul, J., Omri, K., El Mir, L., Barthou, C., and Alaya, S., Journal of Luminescence, 132 (2012) 2288.

[9] Jaballah, S., Benamara, M., Dahman, H., Ly, A., Lahem, D., Debliquy, M., and El Mir, L., Materials Chemistry and Physics, 255 (2022) 123643.

[10] Franco, A. and Pessoni, H.V., Materials Letters, 180 (2016) 305.

[11] David, P.S., Panigrahi, P., and Nagarajan, G.S., Materials Letters, 249 (2019) 9.

[12] El Mir, L., Journal of Inorganic and Organometallic Polymers and Materials, 31 (2021) 2648.

[13] Mahmood, K. and Khalid, A., Materials Letters, 224 (2018) 78.

[14] El Mir, L., Journal of Luminescence, 186 (2017) 98.

[15] Koleva, M.E., Atanasov, P.A., Nedialkov, N.N., Fukuoka, H., and Obara, M., Applied Surface Science, 254 (2007) 1228.

[16] Fu-Chun, Z., Zhi-Yong, Z., Wei-Hu, Z., Jun-Feng, Y., and Jiang-Ni, Y., Chinese Physics Letters, 26 (2009) 16105.

[17] Hong, N.H,, Sakai, J., and Hassini, A., Matter, 17 (2005) 199.

[18] Gao, G.Y., Yao, K.L., and Liu, Z.L., Physics Letters A, 359 (2006) 523.

[19] Xu, C., Yang, K., Huang, L., Liu, Y., and Wang, H., Journal of Physics D: Applied Physics, 41 (2008) 195005.

[20] Vyatkin, A.F., Zinenko, V.I., Agaphonov, Y.A., Pustovit, A.N., Roshchupkin, D.V., Reuss, F., Kirchner, C., Kling, R., and Waag, A., Nuclear Instruments and Methods in Physics Research Section B: Beam Interactions with Materials and Atoms, 237 (2005) 179.

[21] Qi, M., Hou, Q., Sha, S., and Chen, M., Materials Science in Semiconductor Processing, 131 (2021) 105857.

[22] Mrabet, S., Ihzaz, N., Alshammari, M., Khlifi, N., Ba, M., Bessadok, M.N., Mejri, I.H., and El Mir, L., Journal of Alloys and Compounds, 920 (2022) 165920.

[23] Mrabet, S., Ihzaz, N., Bessadok, M.N., Vázquez-Vázquez, C., Alshammari, M., and El Mir, L., Journal of Inorganic and Organometallic Polymers and Materials, 34 (2024) 2064.

[24] Omri, K., Gouadria, S., Madani, M., Mnefgui, S., Alonizan, N., and Alharbi, F., Journal of Materials Science: Materials in Electronics, 34 (2023) 444.

[25] Benamara, M., Teixeira, S.S., Graça, M.P.F., Valente, M.A., Jakka, S.K., Dahman, H., Dhahri, E., El Mir, L., Debliquy, M., and Lahem, D.S., Applied Physics A: Materials Science Processing, 127 (2021) 1.

[26] Williamson, G.K. and Hall, W.H., Acta Metallurgica, 1 (1953) 22.

[27] Mahmoud, A., Echabaane, M., Omri, K., El Mir, L., and Ben Chaabane, R., Journal of Alloys and Compounds, 786 (2019) 960.

[28] Dhahri, R., Hjiri, M., El Mir, L., Bonavita, A., Iannazzo, D., Leonardi, S.G., and Neri, G., Applied Surface Science, 355 (2015) 1321.

[29] Omri, K., Najeh, I., Dhahri, R., El Ghoul, J., and El Mir, L., Microelectronic Engineering, 128 (2014) 53.

[30] Marotti, R.E., Giorgi, P., Machado, G., and Dalchiele, E.A., Solar Energy Materials & Solar Cells, 90 (2006) 2356.

[31] Raghavendra, P.V., Bhat, J.S., and Deshpande, N.G., Materials Science in Semiconductor Processing, 68 (2017) 262.

[32] Park, K., Hakeem, D.A., Pi, J.W., and Jung, G.W., Journal of Alloys and Compounds, 772 (2019) 1040.

[33] Yakout, S.M., Solid State Sciences, 83 (2018) 207.

[34] Kumawat, A., Chattopadhyay, S., and Misra, K.P., Materials and Technology, 38 (2023) 2253646.

[35] Belkhaoui, C., Mzabi, N., Smaoui, H., and Daniel, P., Results in Physics, 12 (2019) 1686.

[36] Safeen, A., Safeen, K., Shafique, M., Iqbal, Y., Ahmed, N., Rauf Khan, M.A., Asghar, G., Althubeiti, K., Al Otaibi, S., Ali, G., Shah, W.H., and Khan, R.T., RSC Advances, 12 (2022) 11923.

[37] Varghese, N., Panchakarla, L.S., Hanapi, M., Govindaraj, A., and Rao, C.N.R., Materials Research Bulletin, 42 (2007) 2117.

[38] Kumar, N., Dorfman, A., and Hahm, J-I., Journal of Nanoscience and Nanotechnology, 5 (2005) 1915.

[39] Srinet, G., Kumar, R., and Sajal, V., Journal of Applied Physics, 114 (2013) 33912.

[40] Ali, R.N., Naz, H., Li, J., Zhu, X., Liu, P., and Xiang, B., Journal of Alloys and Compounds, 744 (2018) 90.

[41] Teke, A., Özgür, Ü., Doğan, S., Gu, X., Morkoç, H., Nemeth, B., Nause, J., and Everitt, H.O., Physical Review B, 70 (2004) 195207.

[42] Vanheusden, K., Seager, C.H., Warren, W.L., Tallant, D.R., and Voigt, J.A., Applied Physics Letters, 68 (1996) 403.

[43] van Dijken, A., Meulenkamp, E.A., Vanmaekelbergh, D., and Meijerink, A., Journal of Physical Chemistry B, 104 (2000) 1715.

[44] Lin, B., Fu, Z., and Jia, Y., Applied Physics Letters, 79 (2001) 943.

[45] Zhao, Q.X., Klason, P., Willander, M., Zhong, H.M., Lu, W., and Yang, J.H., Applied Physics Letters, 87 (2005) 211912.

[46] Studenikin, S.A., Golego, N., and Cocivera, M., Journal of Applied Physics, 84 (1998) 2287.

[47] El Mir, L., Amlouk, A., Barthou, C., and Alaya, S., Physica B: Condensed Matter, 388 (2007) 412.

[48] Ravichandran, K., Karthika, K., Sakthivel, B., Jabena Begum, N., Snega, S., Swaminathan, K., and Senthamilselvi, V.T., Journal of Magnetism and Magnetic Materials, 358–359 (2014) 50.

[49] Luo, X., Lee, W-T., Xing, G., Bao, N., Yonis, A., Chu, D., Lee, J., Ding, J., Li, S., and Yi, J., Nanoscale Research Letters, 9 (2014) 625.

[50] Jayakumar, O.D., Salunke, H.G., Kadam, R.M., Mohapatra, M., Yaswant, G., and Kulshreshtha, S.K., Nanotechnology, 17 (2006) 1278.

[51] Manh, T.V., Phan, T.L., Lee, B.W., Liu, C., Ho, T.A., Thanh, T.D., Vuong, N.M., and Yu, S.C., IEEE Transactions on Magnetics, 51 (2015) 1.

[52] Shatnawi, M., Alsmadi, A.M., Bsoul, I., Salameh, B., Alna'washi, G.A., Al-Dweri, F., and El Akkad, F., Journal of Alloys and Compounds, 655 (2016) 244.

[53] Shatnawi, M., Alsmadi, A.M., Bsoul, I., Salameh, B., Mathai, M., Alnawashi, G., Alzoubi, G.M., Al-Dweri, F., and Bawa'aneh, M.S., Results in Physics, 6 (2016) 1064.

[54] Kalita, A., Current Applied Physics, 52 (2023) 65.

[55] Sarkar, B.J., Deb, A.K., and Chakrabarti, P.K., RSC Advances, 6 (2016) 6395.

[56] Potashnik, S.J., Ku, K.C., Mahendiran, R., Chun, S.H., Wang, R.F., Samarth, N., and Schiffer, P., Physics Review B, 66 (2002) 12408.

[57] Sarkar, B.J., Bandyopadhyay, A., Mandal, J., Deb, A.K., and Chakrabarti, P.K., Journal of Alloys and Compounds, 656 (2016) 339.